nature climate change

Article https://doi.org/10.1038/s41558-025-02537-1

Channelized melt beneath Antarctic ice shelves previously underestimated

Received: 26 July 2024

Accepted: 4 December 2025

Published online: 09 January 2026

Check for updates

Ann-Sofie P. Zinck[1,4] ✉, Stef Lhermitte[1,2], Martin G. Wearing[3] & Bert Wouters[1]

While of critical importance for coastal communities, Antarctica's future sea-level contribution remains highly uncertain. This uncertainty largely stems from the complex interaction between the ocean and the ice shelves, which is both difficult to observe and model. To better understand and constrain land-ice response to reduced buttressing exerted by ice shelves, efforts are needed to fully comprehend basal melt rates and their impact on ice shelf weakening and retreat. Here we present high-resolution basal melt maps (50 m) of vulnerable ice shelves based on a combination of stereo imagery and satellite altimetry, revealing pronounced channelized melting patterns whose melt rates were previously substantially underestimated (42–50%), which could result in faster channel breakthrough. Accurately simulating small-scale dynamics in ice-sheet models remains challenging but is essential for accurate sea-level rise projections.

The evolution of the Antarctic ice sheet poses a major uncertainty in sea-level rise projections, driven largely by the uncertain response of its ice shelves and tributary glaciers to atmospheric and oceanic forcing in a changing climate[1–4]. Ice-shelf thinning and weakening due to basal and surface melting affect the timing and magnitude of ice mass loss as they directly impact the ability of the ice shelf to buttress inland ice[1,4,5]. In a warming climate, as the risk of reduced ice-shelf buttressing increases, certain regions of the ice sheet could become vulnerable to irreversible mass loss[1]. The primary contributors to ice shelf vulnerability are surface and basal melting and damage (crevasses and fracturing). Basal melting is a key concern, as increasing ocean temperatures—with some projections suggesting up to a tripling of historical levels over the twenty-first century—along with potential changes in ocean circulation, are expected to intensify subsurface heat transport towards the ice shelves in the future[4–6].

Repeat observations of change in ice-shelf surface elevation from satellite altimeters have enabled the estimation of basal melt rates for most Antarctic ice shelves at a resolution of 500 m to 1 km (refs. 7,8), revealing that basal melting not only varies in time[7], but is also the primary contributor to mass reduction in ice shelves experiencing the highest losses[8]. Meanwhile, studies of individual ice shelves have shown that combining satellite stereo imagery with altimetry enables substantially higher resolution estimates of basal melting (32–50 m)[9], uncovering previously unseen small-scale features, such as spatial variability within the melt channel of the Dotson ice shelf[9,10]. This improved level of detail, missed in earlier altimetry-only products[11], offers valuable insights into the processes driving basal melting and the potential consequences for ice shelf vulnerability.

Basal melting of ice shelves typically initiates at deep grounding zones and extends into basal channels, where plumes carve troughs in the ice base[12,13]. Basal channels are widespread in Antarctica, particularly in warm-cavity ice shelves[12], yet only a few have been thoroughly studied for their spatial[10,14] and temporal[14,15] variations and their effect on ice shelf integrity[13,14,16]. Studies modelling the ice shelf response to basal melting suggest that high melt rates in basal channels can lead to a complete breakthrough[17,18]. Although so far there are no observations of channel breakthrough solely driven by basal melt, there is evidence of channel incisions leading to large-scale fracturing and ice shelf retreat[13,16,19].

There are many important aspects of basal channel evolution that are not fully understood, such as the feedback with ice shelf fracturing and details of ocean melting (and freeze-on) in channels[13]. However, improved observations of melt patterns in basal channels is crucial to quantify ongoing change and validating models.

[1]Department of Geoscience and Remote Sensing, Delft University of Technology, Delft, the Netherlands. [2]Department of Earth & Environmental Sciences, KU Leuven, Leuven, Belgium. [3]ESRIN, European Space Agency, Rome, Italy. [4]Present address: Physics of Ice, Climate and Earth, Niels Bohr Institute, University of Copenhagen, Copenhagen, Denmark. ✉e-mail: ann-sofie.zinck@nbi.ku.dk

Here we present a high-resolution (50-m posting) basal melt rate product covering several ice shelves, with a focus on those undergoing rapid melt[7,8], located in regions of high ice-mass loss[8] and a high sea-level rise potential[20]. Ice shelves in these regions have the highest observed basal channel density[12], making them especially vulnerable to channel-induced instability. We obtain basal melt rates by combining stereo imagery and satellite altimetry, revealing that altimetry-only estimates often underestimate melt in vulnerable areas. We also discuss the impact of this underestimation on channel breakthrough and ice shelf weakening.

Underestimated channelized melting

We compute ice shelf basal melting for the period 2010–2017, by combining stereo imagery from the reference elevation model of Antarctica (REMA) and CryoSat-2 altimetry using a mass-conservation approach. This approach—basal melt rates using REMA and Google Earth Engine (BURGEE; Methods)—has been used previously to generate high-resolution basal melt rates of the Dotson ice shelf[10].

We compare BURGEE melt rates with those of two altimetry-only studies; ref. 7 (500-m resolution) and ref. 8 (1-km resolution). Both make use of CryoSat-2 radar altimetry to obtain surface-elevation changes. Opposed to the classical point-of-closest-approach method used by ref. 7, another study[8] uses a swath processing[21] which allows for increased spatial detail and coverage. BURGEE and the two altimetry studies are based on the concept of mass conservation in a Lagrangian framework (Methods), which indicates that uncertainties related to factors other than the Lagrangian elevation change (for example, surface mass balance and firn correction) are common across all products (Supplementary Discussion 2). Furthermore, all three methods assume hydrostatic equilibrium, which might be violated in the immediate vicinity of the grounding zone and hence might locally lead to overestimated melt rates.

Our results show that broad-scale (~10 km) ice shelf melt spatial patterns and magnitudes generated by BURGEE are consistent with those observed in earlier altimetry-only studies[7,8] (Extended Data Fig. 1 and Supplementary Fig. 1). The ice shelf integrated total basal melt rate is comparable between all three products, with the exception of Pine Island, where BURGEE produces total melt rates 50% higher than ref. 8 and 90% higher than ref. 7. The enhanced spatial detail of BURGEE reveals more pronounced channelized melting (for example, Moscow University and Totten) and agrees with earlier results based on stereo imagery and altimetry for Pine Island ice shelf[9] (Supplementary Fig. 2).

Basal channels are expressed at the surface as depressions[14]. Since the return echo of radar altimeters such as CryoSat-2 naturally comes from the nearest terrain points, surface depressions may be obscured and undersampled when surrounded by substantially higher terrain, leading to an underestimate of melting (Supplementary Fig. 3). This can for instance be seen near the grounding zone of Drygalski ice shelf, which is unseen by CryoSat-2 because of the surrounding mountains (Supplementary Fig. 1). This could, further, explain the higher BURGEE total melt rate of Pine Island, where melting in along-flow channels dominates the melting signal (Extended Data Fig. 1 and Supplementary Fig. 1). Such limitations are critical, given the importance of small-scale features for comprehensively understanding complex basal melting and its repercussions on ice shelf vulnerability. Although the use of swath processing[21] in ref. 8 enables increased spatial detail as compared with ref. 7, it does not fully resolve the problem of undersampling deep surface depressions. The extent of underestimated melting is illustrated in Extended Data Fig. 2, where BURGEE reveals higher third-quartile melt rates than both ref. 8 (8 m yr^{-1} versus 4 m yr^{-1}) and ref. 7 (8 m yr^{-1} versus 5 m yr^{-1}) across areas where the ice shelf is thin (0–200 m). Thin-ice areas often contain fractures and also coincide with the location of basal channels, such as the downstream section of the main basal channel on Dotson, and thus represent some of the weakest areas on the ice shelves (Extended Data Fig. 3). BURGEE shows higher third-quartile melt rates for all ranges of ice thickness up to 1,000 m. This holds in particular for the thinnest ice (200–400 m; 6 m yr^{-1} compared with 5 m yr^{-1} and 4 m yr^{-1} for ref. 7 and ref. 8, respectively). Considering all studied ice shelf areas where ice thickness ranges from 200 m to 400 m, BURGEE reveals higher third-quartile melt rates (6 m yr^{-1}) than both ref. 7 (5 m yr^{-1}) and ref. 8 (4 m yr^{-1}). The similar distributions of BURGEE on a 50-m and 500-m posting show that underestimating melting is not a consequence of the product grid size (ref. 7 at 500 m and ref. 8 at 1 km).

Furthermore, a Fourier analysis of the basal melt maps shows that only BURGEE explores the full range of basal-melting wavelengths, which suggests that BURGEE, unlike the altimetry-only studies, captures all melting present within the signal. This finding does not only support the potential underestimation of channelized melting, but also provides a wavelength (500 m) at which basal melting (or its impact) should be resolved in models (Methods; Supplementary Fig. 4). Finally, secondary-flow processes are not (fully) considered in any of the three basal melting products, suggesting that true peak melt rates may be even more underestimated.

Channel breakthrough

Basal channels in thin-ice areas (<600 m) that are subject to high melt rates are at risk of channel breakthrough[17]. Calculating breakthrough times offers a framework to indirectly assess structural vulnerability, as high channel incision in thin ice may trigger further damage[13,16,19]. We therefore examine how enhanced channelized melting, revealed by BURGEE, influences channel breakthrough in these potentially vulnerable zones in ice shelves. Linearly extrapolating channel melt rates have previously been used to estimate channel breakthrough times[11]. However, modelling work using a full-Stokes ice-flow model with idealized basal melting demonstrates that channel incision can be slowed—and in some cases prevented—by secondary flow, that is, the viscous inflow of ice towards the channel centre induced by the gradient in ice thickness between the channel and the surrounding ice shelf[17]. The modelling results[17] show that the primary factors influencing the time to approach breakthrough are the peak melt rate within the channel and the ice shelf thickness outside the channel[17]. In areas with thick ice (>600 m), secondary flow can balance melting and prevent channel incision. In areas of thinner ice (<600 m), where secondary flow cannot prevent channel breakthrough, the peak melt rate is a dominant control on how fast channels approach breakthrough. The fracturing aspect of breakthrough can be simulated with models that include fracture-specific physics (such as refs. 22,23). The breakthrough time of a channel, and consequently the stability of the ice shelf, thus depend on the imbalance between the peak melt rate within the channel and secondary flow induced by ice thickness gradients.

To understand the implications of previously underestimated channelized melt rates on channel breakthrough times and vulnerability, we identify channels on all ice shelves included in this study (Methods and Extended Data Fig. 3). Channels with high slopes (maximum slopes >15°; Methods), which often coincide with damage (rifting and crevasses; Supplementary Fig. 5), are excluded (Extended Data Fig. 3). We focus on a subset of the slope-limited channels, namely those (labelled studied channels in Extended Data Fig. 3) that are subject to high melt rates (90% percentile >10 m yr^{-1}; Methods), as they potentially have a high likelihood of breaking through. The outflow of the detected channels aligns well with the location of known persistent polynyas[24] (Extended Data Fig. 3), indicators of buoyant upwelling from channelized meltwater[25], except for the easternmost polynya near Pine Island ice shelf, an area of recent ice shelf retreat.

Since channel incision and potential breakthrough are controlled by peak melt rates within channels, we extract and compare the localized peak melt rates within all studied channels from BURGEE, ref. 7 and ref. 8 (Methods and Supplementary Fig. 6). BURGEE indeed reveals higher melting in channels (Supplementary Fig. 6), with altimetry-only peak melt rates underestimated substantially by up to 42% for ref. 8 and

50% for ref. 7, probably because the deep surface depressions resolved by REMA are not (fully) captured by CryoSat-2. To assess whether the underestimated melt in the altimetry-only studies is general across channels, or only at the deepest surface depressions, we extract mean melt rates along 10-km transects transverse to the channels (Methods). The mean melt rates across channels are on average underestimated by 11% for ref. 8 and 22% for ref. 7, showing that melting underestimation is present across channels, although more severe at the deepest surface depressions.

The underestimation of peak melt rates is consistent across all ice shelves and ice shelf thicknesses studied (Extended Data Fig. 4). Since this underestimation has consequences for assumptions about ice shelf vulnerability, we assess the impact of increased peak melt rates in an idealized model using the normalized breakthrough times (NBTs) as an indicator of vulnerability. The NBT describes the breakthrough slow-down due to secondary flow and is defined as the time for a channel to breakthrough when secondary flow is considered divided by the linear breakthrough time[17] (Extended Data Fig. 4). The NBT relationship is derived from an idealized two-dimensional (2D) cross-section of an ice shelf made for channels with a characteristic channel width of 2.5 km (Methods).

The higher BURGEE peak melt rates yield shorter NBTs across all ice shelves studied (Extended Data Fig. 4) when compared with both altimetry-only studies[7,8]. This conclusion would not change for narrower (wider) channels, which have longer (shorter) NBTs, as breakthrough time is still controlled by the peak melt rate[17].

The implications of underestimating peak melt rates and shorter NBTs are evident on Pine Island and Dotson/Crosson ice shelves, where channel dimensions resemble those in the modelling study[17] (characteristic channel width 1.5–3.5 km, ice thickness <1,000 m, peak melt rate 8–50 m yr^{-1}). Within the most downstream part of the main melt channel on Dotson (lime box, Supplementary Fig. 8a), peak melt rate and breakthrough time with secondary flow of BURGEE (16.6 ± 0.8 m yr^{-1} and 7 ± 1 yr) match results from ref. 8 (15.1 ± 0.6 m yr^{-1} and 7 ± 1 yr) but are twice as high/fast as those from ref. 7 (8.2 ± 1.0 m yr^{-1} and 13 ± 2 yr). For the thicker ice upstream the main melt channel (orange box), BURGEE peak melt rate (28.9 ± 2.3 m yr^{-1}) and breakthrough time with secondary flow (17 ± 1 yr) are several times higher/faster than reported by both ref. 8 (15.5 ± 0.3 m yr^{-1} and 94 ± 3 yr) and ref. 7 (14.5 ± 0.9 m yr^{-1} and 100 ± 7 yr). On the Pine Island western shear zone (red box), BURGEE shows 17.1 ± 2.2 m yr^{-1} peak melt and 25 ± 3 yr breakthrough, while ref. 8 (2.8 ± 0.7 m yr^{-1}) and ref. 7 (6.2 ± 0.5 m yr^{-1}) predict rates too low for channel breakthrough.

Reduced breakthrough times have notable consequences if the breakthrough time is shorter than the residence time, that is, the time that it takes for the ice to advect to the ice shelf front. On Dotson/Crosson, all channels, except a subsection at the Crosson–Dotson shear zone (turquoise box, Supplementary Fig. 8), have the potential to breakthrough (Supplementary Fig. 8 and Methods). By contrast, neither ref. 7 nor ref. 8 results exhibit melt rates high enough to cause a breakthrough in major sections of the Dotson main melt channel (yellow and olive boxes, Supplementary Fig. 8). On other parts of the main channel (orange box, Supplementary Fig. 8) their breakthrough times (94 ± 3 yr and 100 ± 7 yr) are much closer to the residence time (147 yr) than BURGEE (17 ± 1 yr).

On the fast-flowing Pine Island ice shelf, where residence times are amongst the shortest in Antarctica, basal channel breakthrough is possible for two channels in the eastern shear zone (BURGEE breakthrough time, 12 ± 2 yr; residence time, 13 yr; purple box, Supplementary Fig. 8) and west of the western shear zone (BURGEE breakthrough time, 11 ± 1 yr; residence time, 45 yr; blue box, Supplementary Fig. 8). However, irrespective of residence time, these channels would not breakthrough when considering the lower ref. 7 peak melt rates (<8 m yr^{-1}). Using ref. 8 melt rates, only the eastern channel (purple box, Supplementary Fig. 8) has the potential to breakthrough, although not within its residence time.

The only channel on Pine Island where channel breakthrough is unlikely (25 ± 3 yr BURGEE peak melt versus 8 yr residence time) is located in the western shear zone of the ice shelf (red box, Supplementary Fig. 8). Here extensive damage has already caused calving and ice shelf retreat[22]. On several other ice shelves, similar transverse fracturing has been observed in the vicinity of basal channels[19] (that is, Nansen, Moscow University, Totten). Monitoring such areas at high resolution is therefore crucial to understand the interplay between basal melt channels, damage and their role in calving and ice shelf retreat, and highlights the importance of considering channel breakthrough times as indicator for future damage development.

Discussion

The previous underestimation of peak melt rates in ice shelf basal channels has implications for assessing how channels evolve, but the direct link to large-scale instability or imminent channel breakthrough warrants further investigation, especially given the simplicity and idealized nature of the model framework used here. Our results thus illustrate the potential sensitivity of channel breakthrough times to underestimated melt rates, but does not constitute a prediction of breakthrough occurrence or timing. Our findings highlight the importance of accurately resolving basal melt rates, particularly at small scales, but also underline that more comprehensive modelling, including full three-dimensional (3D) ice dynamics, fracture physics and coupled ocean–ice interactions, is required before substantial conclusions about breakthrough and long-term stability can be drawn. While melt rates derived from altimetry-only observations are not fully capable of constraining channel melt patterns, they do have the advantage of a higher temporal resolution, as they are not constrained to cloud-free and sunlit conditions, which are needed for stereo imagery. There is an opportunity to obtain channel melt rates at high spatiotemporal resolution using a combination of altimetry and high-resolution digital elevation models (DEMs) through data fusion[26] or deep learning, as has been done for surface melt[27].

Our findings point to the need for careful reassessment of Antarctic ice shelf vulnerability, explicitly accounting for small-scale basal channel ocean dynamics and ice shelf mechanics. Here we have used a simplified model representation of basal channel evolution to consider the implications of increased peak melt rates, neglecting 3D ice dynamics, channel width variability, elastic and brittle deformation, spatiotemporal evolution of melting and uncertainty related to ice-flow parameters. However, to fully assess the implications of focused melting in basal channels and project future change, these processes should be included in ice-sheet models. Crucially, basal channels must be simulated at high resolution (≤500 m) to capture channel evolution and interplay with fractures. Furthermore, there is a need to accurately simulate ocean dynamics and melting within basal channels in a coupled ocean model. Ongoing efforts aim to include those processes in simulations with realistic[28] and idealized geometries[18,29–31]. However, integrating them into ice-sheet-wide projections is essential to fully evaluate the impact of ocean melting on ice-sheet stability and the implications for global sea-level rise[32].

Online content

Any methods, additional references, Nature Portfolio reporting summaries, source data, extended data, supplementary information, acknowledgements, peer review information; details of author contributions and competing interests; and statements of data and code availability are available at https://doi.org/10.1038/s41558-025-02537-1.

References

1. Pattyn, F. et al. The uncertain future of the Antarctic Ice Sheet. *Science* **367**, 1331–1335 (2020).
2. IPCC. *Climate Change 2021: The Physical Science Basis* (eds Masson-Delmotte, V. et al.) (Cambridge Univ. Press, 2023).

3. Bamber, J. L. et al. Ice sheet and climate processes driving the uncertainty in projections of future sea level rise: findings from a structured expert judgement approach. *Earth's Future* **10**, e2022EF002772 (2022).
4. van de Wal, R. S. W. et al. A high end estimate of sea level rise for practitioners. *Earth's Future* **10**, e2022EF002751 (2022).
5. Pattyn, F. et al. The Greenland and Antarctic ice sheets under 1.5 °C global warming. *Nat. Clim. Change* **8**, 1053–1061 (2018).
6. Naughten, K. A. et al. Unavoidable future increase in West Antarctic ice-shelf melting over the twenty-first century. *Nat. Clim.Change* **13**, 1222–1228 (2023).
7. Adusumilli, S. et al. Interannual variations in meltwater input to the Southern Ocean from Antarctic ice shelves. *Nat. Geosci.* **13**, 616–620 (2020).
8. Davison, B. J. et al. Annual mass budget of Antarctic ice shelves from 1997 to 2021. *Sci. Adv.***9**, eadi0186 (2023).
9. Shean, D. E. et al. Ice shelf basal melt rates from a high-resolution digital elevation model (DEM) record for Pine Island Glacier, Antarctica. *Cryosphere* **13**, 2633–2656 (2019).
10. Zinck, A.-S. P. et al. Unveiling spatial variability within the Dotson melt channel through high-resolution basal melt rates from the reference elevation model of Antarctica. *Cryosphere* **17**, 3785–3801 (2023).
11. Gourmelen, N. et al. Channelized melting drives thinning under a rapidly melting Antarctic ice shelf. *Geophys. Res. Lett.* **44**, 9796–9804 (2017).
12. Alley, K. E. et al. Impacts of warm water on Antarctic ice shelf stability through basal channel formation. *Nat. Geosci.* **9**, 290–293 (2016).
13. Alley, K. E. et al. The role of channelized basal melt in ice-shelf stability: recent progress and future priorities. *Ann. Glaciol.* **63**, 18–22 (2022).
14. Alley, K. E. et al. Evolution of sub-ice-shelf channels reveals changes in ocean-driven melt in West Antarctica. *J. Glaciol.* **70**, e50 (2024).
15. Chartrand, A. M. et al. Basal channel evolution on the Getz Ice Shelf, West Antarctica. *J. Geophys. Res. Earth Surf.* **125**, e2019JF005293 (2020).
16. Chartrand, A. M. et al. Thwaites Glacier thins and retreats fastest where ice-shelf channels intersect its grounding zone. *Cryosphere* **18**, 4971–4992 (2024).
17. Wearing, M. G. et al. Ice shelf basal melt channels stabilized by secondary flow. *Geophys. Res. Lett.* **48**, e2021GL094872 (2021).
18. Humbert, A. et al. On the evolution of an ice shelf melt channel at the base of Filchner ice shelf, from observations and viscoelastic modeling. *Cryosphere* **16**, 4107–4139 (2022).
19. Dow, C. F. et al. Basal channels drive active surface hydrology and transverse ice shelf fracture. *Sci. Adv.* **4**, eaao7212 (2018).
20. Seroussi, H. et al. ISMIP6 Antarctica: a multi-model ensemble of the Antarctic ice sheet evolution over the 21st century. *Cryosphere* **14**, 3033–3070 (2020).
21. Gourmelen, N. et al. CryoSat-2 swath interferometric altimetry for mapping ice elevation and elevation change. *Adv. Space Res.* **62**, 1226–1242 (2018).
22. Lhermitte, S. et al. Damage accelerates ice shelf instability and mass loss in Amundsen Sea Embayment. *Proc. Natl Acad. Sci. USA* **117**, 24735–24741 (2020).
23. Kachuck, S. B. et al. Simulating ice-shelf extent using damage mechanics. *J. Glaciol.* **68**, 987–988 (2022).
24. Alley, K. E. et al. Troughs developed in ice-stream shear margins precondition ice shelves for ocean-driven breakup. *Sci. Adv.* **5**, eaax2215 (2019).
25. Mankoff, K. D. et al. The role of Pine Island Glacier ice shelf basal channels in deep-water upwelling, polynyas and ocean circulation in Pine Island Bay, Antarctica. *Ann. Glaciol.* **53**, 123–128 (2012).
26. Winstrup, M. et al. Prodem: an annual series of summer dems (2019 through 2022) of the marginal areas of the greenland ice sheet. *Earth Syst. Sci. Data* **16**, 5405–5428 (2024).
27. de Roda Husman, S. et al. A high-resolution record of surface melt on Antarctic ice shelves using multi-source remote sensing data and deep learning. *Remote Sens. Environ.* **301**, 113950 (2024).
28. Lambert, E. et al. Modelling Antarctic ice shelf basal melt patterns using the one-layer Antarctic model for dynamical downscaling of ice-ocean exchanges (LADDIE v1.0). *Cryosphere* **17**, 3203–3228 (2023).
29. Sergienko, O. V. Basal channels on ice shelves. *J. Geophys. Res. Earth Surf.* **118**, 1342–1355 (2013).
30. Drews, R. Evolution of ice-shelf channels in Antarctic ice shelves. *Cryosphere* **9**, 1169–1181 (2015).
31. Bassis, J. et al. Evolution of basal crevasses links ice shelf stability to ocean forcing. *Earth Planet. Sci. Lett.* **409**, 203–211 (2015).
32. van Westen, R. M. et al. Ocean eddies strongly affect global mean sea-level projections. *Sci. Adv.* **7**, eabf1674 (2021).

Methods

Basal melt rates using REMA and Google Earth Engine

To calculate the basal melt rates we make use of BURGEE v.2, an updated version of BURGEE v.1[10]. The basal melting is calculated in a Lagrangian reference frame following a mass-conservation approach and under the assumption that the ice shelf is floating in hydrostatic balance. The basal melt rate ($\mathring{M}_b$) is thus obtained through

$$\mathring{M}_b = \mathring{M}_s - \left(\frac{Dh}{Dt} - \frac{Dh_f}{Dt} + (h - h_f)(\nabla \cdot \mathbf{u})\right)\frac{\rho_w}{\rho_w - \rho_i}, \quad (1)$$

where $\mathring{M}_s$ is the mean annual surface mass balance over the study period obtained from the regional climate model RACMO 2.3p3[33], $\frac{D}{Dt}$ denotes the Lagrangian change, h is the surface elevation, h_f is the firn air content obtained from the firn densification model IMAU-FDM v.1.2A[34], ρ_w is the density of water (assumed to be 1,025 kg m^{-3}), ρ_i is the density of ice (assumed to be 917 kg m^{-3}) and $\nabla \cdot \mathbf{u}$ is the divergence of the velocity field. For the last we use the MEaSUREs ITS_LIVE data product[35] and total-variation regularization[36] to calculate the divergence. In the design of BURGEE, no specific site-tuning was applied[10], which suggests that the only limitations of applying BURGEE on other ice shelves are data availability and potentially computational constraints. A full description of BURGEE v.1, including a sensitivity experiment of the Lagrangian displacement, can be found in ref. 10. In the following sections we describe the updates made to achieve BURGEE v.2 (Supplementary Table 1).

Co-registering REMA elevations

We use CryoSat-2 measurements (Level-1B SARin Baseline-E where available and Baseline-D otherwise) to co-register the REMA strips using a plane-fit approach. Before the co-registration takes place, both CryoSat-2 and REMA elevations are referenced to the EGM2008 geoid[37] and corrected for the mean dynamic topography (DTU15MDT), tides (CATS2008) and inverse barometer effect using the 6 h NCEP/NCAR sea-level pressure reanalysis data. In BURGEE v.2, the REMA strips are corrected for tides with pyTMD using the acquisition time of the first stereo image, as opposed to on a 6-hourly basis as in BURGEE v.1. In the co-registration, a few adjustments have been made with respect to the CryoSat-2 coverage over the individual REMA strips, needed to perform the co-registration. In BURGEE v.1 the CryoSat-2 points furthest apart from each other in the latitudinal and longitudinal directions were required to be separated by at least 60 km and 10 km, respectively, to ensure sufficient representation. This criterion has been changed to a CryoSat-2 coverage in both the latitudinal and longitudinal directions of at least 75% of the distance of the REMA strip in both of those directions. This indicates that even small REMA strips, that otherwise would have been filtered out, will be taken into consideration, while making sure that we have a sufficient CryoSat-2 coverage. Furthermore, the minimum number of CryoSat-2 points needed was previously set to 80; this has now been changed to at least 80 points or at least a 5% CryoSat-2 coverage at a 500-m resolution. As for the latitudinal and longitudinal coverage criterion, this change suggests that smaller, otherwise good quality, REMA strips are not filtered out.

Lagrangian elevation change and basal melt rate

To obtain the Lagrangian elevation change, all REMA strips are displaced to their 2017-01-01 location based on the ITS_LIVE velocities[35] and are further displaced using feature tracking with respect to the median elevation map based on all velocity-displaced REMA strips from 1 July 2015 to 1 July 2017. In BURGEE v.1, the reference elevation map used was generated from the last year of data only, however, not all ice shelves in this study have equally good coverage in the last study year (Supplementary Fig. 9), so this ensures better coverage and therefore more features which can be used in the feature tracking. Furthermore, in BURGEE v.2 we apply the feature tracking to all strips individually instead of first generating yearly median elevation maps. Yearly median elevation maps are generated after the final displacement, and only years covering at least 25% of an ice shelf are used, since years with limited coverage reduces the quality of the basal melt rate estimation. Finally, for the same reason, the basal melt rate in BURGEE v.2 is only calculated in pixels with at least 3 years of elevation coverage (Supplementary Fig. 9 gives a full overview of areas covered per year). Remote sensing-derived basal melt rates should always be used with care in the vicinity of the grounding line, since hydrostatic equilibrium assumptions can interfere with the inferred melting signal. Ice shelves experiencing grounding line retreat are therefore more sensitive to interferences in the melting signal in the vicinity of the grounding line, with its spatial implications determined by ice flow.

Model description

We use the idealized modelling results from ref. 17 to assess the time to approach breakthrough (as a metric for structural vulnerability). This idealized modelling considers a confined 2D vertical plane, of 50-km width, aligned perpendicular to a basal channel. The full-Stokes numerical ice-flow model ELMER/Ice[38] is used to simulate the evolution of a basal channel. The domain is assumed to be advected in the primary flow direction of the ice shelf, without along-flow extension. An idealized basal melt rate is imposed at the centre of the domain using a Gaussian function with peak melt rate (M_p) and a characteristic width (x_m, equal to 1 s.d.). Surface accumulation is spatially uniform and set so that the total accumulation matches the total basal melting. The ice rheology is specified by Glen's flow law, with a uniform rate factor appropriate for ice at −10 °C, ($A = 3.5 \times 10^{-25}$ s^{-1} Pa^{-3})[39] and flow-law exponent $n = 3$. Each simulation is initiated with an ice shelf of uniform thickness (H) and is run for one characteristic time. If the channel incises completely the simulation stops. The results used in this assessment use a characteristic width of $x_m = 2{,}500$ m.

This idealized modelling neglects some more complex processes, such as the effect of longitudinal and transverse strain (determined by local and ice shelf scale stresses) on ice shelf thickness and effective viscosity, elastic deformation, brittle deformation, fine-scale and spatiotemporal evolution of ice–ocean interaction (melting and freeze-on).

Extracting channels

Under the assumption that the ice shelf surface topography reflects that of the ice shelf base, we use the surface topography to systematically identify the location of basal channels. Using the REMA DEM mosaic[40] at 32-m resolution, bicubic downsampled onto a 250-m resolution grid, we calculate the accumulated flow in each grid cell. The accumulated flow is the number of upstream cells calculated using a watershed delineation approach (pysheds). We define basal channels as grid cells with an upstream inflow of at least 1,000 cells. This threshold was found through trial-and-error, with the goal of removing as many 'visually false' channels as possible, while keeping 'visually true' channels. A comparison with other thresholds is shown in Supplementary Fig. 10, which shows that the end product of 'studied channels' is little influenced by this threshold. To exclude smaller sub-branches, channels shorter than 2.5 km are filtered out, together with those shorter than 10 km if the maximum accumulated flow of the channel is less than 5,000 upstream pixels. We refer to the resulting channels as 'all channels' (Extended Data Fig. 3) and compare them to existing channel products (Supplementary Fig. 11). We, furthermore, perform a sensitivity test by varying these thresholds within reasonable bounds, which shows only little dependence on their actual value (Supplementary Fig. 12). To exclude crevasses, which otherwise fulfilled the aforementioned criteria, we filter out channels where the maximum slope (considering both along and across flow) is greater than 15°. These channels that are filtered out correspond to either channels in highly fractured areas or actual fractures (Supplementary Fig. 5). While recent studies do show elevated melt rates within crevasses[41,42], it is difficult to fully separate the elevation change signal into components associated with fracturing and basal melting. The remaining channels are referred to as 'slope-corrected channels' (Extended Data Fig. 3). Finally, in this study we only consider a subset of the slope-corrected channels, namely those channels with at least 50% BURGEE coverage and with a 90% percentile melt rate higher than 10 m yr^{-1}, which we consider indicative of channels with active melting. These channels are referred to as 'studied channels' (Extended Data Fig. 3).

Peak channel melt rates and breakthrough analysis

To analyse melting within the channels, we extract 10-km transects perpendicular to the channels at 1-km intervals along their length (Supplementary Fig. 13). Since channel breakthrough times depend on ice thickness, we divide the channels into segments (subchannels) on the basis of their ice thickness. This segmentation ensures that representative values for peak melt rates, mean melt rates and ice thickness are used in the breakthrough analysis. The segmentation is based on the difference in along-channel thickness (ΔH). The thickness bin size (H_{bin}) is calculated as

$$H_{\text{bin}} = \frac{\Delta H}{\lceil \Delta H/100 \rceil}, \tag{2}$$

where ⌈ ⌉ is the ceiling function. This method ensures bin intervals are a maximum of 100-m ice thickness (example in Supplementary Fig. 13). Subchannels comprising less than three transects are excluded from the analysis.

For each subchannel, we extract median transects of BedMachine v.3 ice thickness[43], REMA surface elevations[40] and basal melt rates from BURGEE, ref. 7 and ref. 8, respectively. Channel widths are derived for each transect by averaging the surface-elevation profile of the transect and its mirrored counterpart, fitting an inverted Gaussian curve at the channel centre and using the first two maxima to define channel boundaries (Supplementary Fig. 13). The standard deviation of the Gaussian fit is defined as the characteristic channel width. Subchannels with standard deviations exceeding 10 km are excluded as outliers, as they suggest basal channels wider than 10 km. These wide channels are typically located in regions where REMA surface depressions are poorly represented in BedMachine v.3 owing to its coarser resolution (500 m) or because of differences in the BedMachine v.3 input data, as it is not solely based on the REMA mosaic. Additionally, subchannels with more than 20% grounded ice within their median transects are excluded, as the assumption of hydrostatic equilibrium becomes invalid near the grounding line.

To determine representative values for ice thickness and melt rates, we define the ice shelf thickness outside the channel as the 80% percentile of the median ice thicknesses across all transects (Supplementary Fig. 13). Peak melt rates are calculated as the 90% percentile of transect melt rates within ±2 km of the channel centre (that is, the channel positions as derived from the accumulated flow analysis, Supplementary Fig. 13). Mean channel melt rates are defined as the average of the respective transect median melt rates.

Evaluation of peak melt rates and breakthrough times

We compare the ice thicknesses outside the channels with the channel peak melt rates of all three products (BURGEE, ref. 7 and ref. 8, Extended Data Fig. 4), as these are the main factors influencing channel breakthrough times. We zoom in on the thinner ice sections (200–900 m), where channel breakthrough is possible, even when secondary flow is taken into consideration (Extended Data Fig. 4). For these thinner ice sections, NBTs of channels with a channel width of 1.5–3.5 km are compared between all three products (solid makers in Extended Data Fig. 4). The remaining channels are all narrower than 1.5 km and are not comparable in size to the channel assumptions made in the modelling study to obtain the NBTs[17] (2.5 km). We, furthermore, calculate linear breakthrough times (t_{lb}) using

$$t_{\text{lb}} = H_{\text{c}}/\mathring{M}_{\text{p}}, \tag{3}$$

where H_{c} is the ice thickness within the channel and $\mathring{M}_{\text{p}}$ is the peak melt rate. The linear breakthrough times are of special interest for ice shelves thinner than 400 m where secondary flow barely provides any breakthrough delay[17] (Supplementary Fig. 7b).

Using the linear breakthrough times and NBTs from ref. 17, breakthrough times with secondary flow are calculated. NBTs are only available for channels thinner than 1,000 m and peak melt rates in the range of 8 m yr^{-1} to 50 m yr^{-1}. Ice shelf residence times (the time that it takes for the ice to advect to the ice shelf front) are obtained from ref. 17 and are based on MEaSUREs v.2 ice velocities in comparison to the distance from the ice shelf front. The residence times are compared with the breakthrough times with secondary flow to establish whether a channel is likely to breakthrough before it reaches the ice shelf front.

Finally, we compare the impact of the different time periods the reference maps are based on in the Lagrangian frameworks of the different melt products (Supplementary Figs. 2 and 14) on the peak melt rates and thus also on assumptions about channel breakthrough (Supplementary Figs. 15 and 16).

Wavelength analysis

To determine whether all basal melt products analysed in this study capture the full range of possible melting wavelengths within their signal, including the smaller scales associated with channelized melting, we perform a Fourier analysis of the basal melt maps. Specifically, we assess the Lomb–Scargle spectra[44,45] of the melt maps, a statistical tool designed to detect periodic signals in unevenly spaced data, which accommodates gaps in the maps. For consistency, we restrict the analysis to areas covered by all products.

The melt maps from the three products (BURGEE, ref. 7 and ref. 8) are treated as individual 2D arrays per ice shelf. The analysis is conducted on data rows (or columns) of the individual 2D arrays in segments of 10 km, with an overlap of 5 km between consecutive segments. To minimize spectral leakage, a Hamming window is applied to each segment before performing the Lomb–Scargle analysis. We only include segments with at least 90% data coverage and calculate their power spectra using the following sampling intervals (t) and frequencies (f):

$$t = \{t_0, t_1, t_2, \ldots, t_n\}, \text{ where } t_i = ir \text{ and } t_n < L,\ t_{n+1} \geq L, \tag{4}$$

and

$$f = \{f_0, f_1, f_2, \ldots, f_n\}, \text{ where } f_i = i\frac{1}{L}, \text{ and } f_n < \frac{0.5}{r}, f_{n+1} \geq \frac{0.5}{r}, \tag{5}$$

where i is the index, r is the posting of the product (thus 50 m, 500 m or 1,000 m) and L is the segment length (10 km).

The choice of whether to analyse rows or columns is based on the predominant direction of ice flow and thus the rough 'direction' of melting and channels. For Thwaites, Dotson/Crosson and Drygalsky ice shelves, we analyse the power spectra of all columns to ensure that the melting/channels are roughly perpendicular to the analysed segments. For all other ice shelves, we analyse the power spectra of all rows.

Finally, the power spectra are averaged per product and across all ice shelves, including the BURGEE product at both 50 m and 500 m spatial resolutions, as shown in Supplementary Fig. 4.

Uncertainty estimation

To estimate the uncertainty of the peak melt rates we calculate the standard deviation of melt rates between the 85 and 95 percentiles of all channel transects within a given channel. The uncertainty of the channel ice thickness is calculated by taking the standard deviation of the minimum channel thickness across all channel transects within a channel. The uncertainty estimations of linear and secondary-flow breakthrough times are obtained through error propagation, in which we assume that the NBTs are not associated with any errors as they are the result of an idealized model set up designed to represent a generic channel. Uncertainties in the residence time are associated with errors in the velocity product used and the calving front position (which may change with iceberg calving events). For ice shelves, the uncertainties are relatively low (approximately <1% of flow speed) and we, therefore, consider them to be negligible.

Data availability

The derived channel product and BURGEE basal melt rates are publicly available (https://doi.org/10.4121/4e2ba9a9-7b1b-4837-b52d-036f8c876e67)[46]. REMA strips and mosaics are available from the Polar Geosptaital Center (https://www.pgc.umn.edu/data/rema/), CryoSat-2 data are available from the European Space Agency (https://earth.esa.int/eogateway/documents/20142/37627/CryoSat-Baseline-D-Product-Handbook.pdf) and MEaSUREs ITS_LIVE velocities and BedMachine v.3 are both available from NASA National Snow and Ice Data Center (https://doi.org/10.5067/6II6VW8LLWJ7 and https://nsidc.org/data/NSIDC-0756/versions/3). The ref. 8 basal melt product is available via Zenodo at https://doi.org/10.5281/zenodo.8052519 (ref. 47) and the melt product from ref. 7 is available from UC San Diego (https://doi.org/10.6075/J04Q7SHT). The ice shelf damage product is available from the 4TU research data repository (https://doi.org/10.4121/911e8799-f0dc-42e3-82b4-766ad680a71e.v2). The polynyas and manually derived channels from ref. 12, the basal melt rates of Pine Island from ref. 9 and the model results of the impact of secondary flow on channel breakthrough from ref. 17 are available from the respective authors on request.

Code availability

The BURGEE code (v.1 and v.2) is publicly available (https://github.com/aszinck/BURGEE)[48] and code for the channel analysis and deriving channels is available via Zenodo at https://doi.org/10.5281/zenodo.17671626 (ref. 49).

References

33. van Wessem, J. M. et al. Modelling the climate and surface mass balance of polar ice sheets using RACMO2—Part 2: Antarctica (1979–2016). *Cryosphere* **12**, 1479–1498 (2018).
34. Veldhuijsen, S. B. M. et al. Characteristics of the 1979–2020 Antarctic firn layer simulated with IMAU-FDM v1.2A. *Cryosphere* **17**, 1675–1696 (2023).
35. Gardner, A. et al. *MEaSUREs ITS_LIVE Regional Glacier and Ice Sheet Surface Velocities* version 1, https://nsidc.org/data/nsidc-0776/versions/1 (NASA, 2022).
36. Chartrand, R. *Numerical Differentiation of Noisy, Nonsmooth, Multidimensional Data* 244–248 (IEEE, 2017).
37. Pavlis, N. K. et al. The development and evaluation of the Earth Gravitational Model 2008 (EGM2008). *J. Geophys. Res. Solid Earth* **117**, B04406 (2012).
38. Gagliardini, O. et al. Capabilities and performance of Elmer/Ice, a new-generation ice sheet model. *Geosci. Model Dev.* **6**, 1299–1318 (2013).
39. Cuffey, K. M. & Paterson, W. *The Physics of Glaciers* 4th edn (Elsevier, 2010).
40. Howat, I. M. et al. The reference elevation model of Antarctica. *Cryosphere* **13**, 665–674 (2019).
41. Schmidt, B. E. et al. Heterogeneous melting near the Thwaites Glacier grounding line. *Nature* **614**, 471–478 (2023).
42. Wåhlin, A. et al. Swirls and scoops: ice base melt revealed by multibeam imagery of an Antarctic ice shelf. *Sci. Adv.* **10**, eadn9188 (2024).
43. Morlighem, M. *MEaSUREs BedMachine Antarctica* version 3, https://nsidc.org/data/NSIDC-0756/versions/3 (NASA, 2022).
44. Lomb, N. R. Least-squares frequency analysis of unequally spaced data. *Astrophys. Space Sci.* **39**, 447–462 (1976).
45. Scargle, J. D. Studies in astronomical time series analysis. II—Statistical aspects of spectral analysis of unevenly spaced data. *Astrophys. J.* **263**, 835–853 (1982).
46. Zinck, A.-S. et al. Dataset belonging to the article: Exposure to underestimated channelized melt in Antarctic Ice Shelves. *4TU.ResearchData* https://doi.org/10.4121/4e2ba9a9-7b1b-4837-b52d-036f8c876e67 (2024).
47. Davison, B. Data and code for: "Annual mass budget of Antarctic ice shelves from 1997 to 2021" [Data set]. *Zenodo* https://doi.org/10.5281/zenodo.8052519 (2023).
48. Zinck, A.-S. BURGEE. *GitHub* https://github.com/aszinck/BURGEE (2023).
49. Zinck, A.-S. Code belonging to the article 'Channelized melt beneath Antarctic ice shelves previously underestimated'. *Zenodo* https://doi.org/10.5281/zenodo.17671626 (2025).
50. Scambos, T. et al. MODIS-based Mosaic of Antarctica (MOA) data sets: continent-wide surface morphology and snow grain size. *Remote Sens. Environ.* **111**, 242–257 (2007).
51. Matsuoka, K. et al. Quantarctica, an integrated mapping environment for antarctica, the southern ocean, and sub-antarctic islands. *Environ. Model. Softw.* **140**, 105015 (2021).

Acknowledgements

This study is a part of the HiRISE project funded by the Dutch Research Council (NWO, no. OCENW.GROOT.2019.091).

Author contributions

The research was designed by A.-S.P.Z., S.L. and B.W. and carried out by A.-S.P.Z. M.G.W. made substantial contributions to the interpretations of the results. The writing of the paper was led by A.-S.P.Z. with input from all authors.

Competing interests

M.G.W. is employed by European Space Agency (ESA) who are responsible for satellite radar altimeter CryoSat-2. ESA had no involvement in the study and did not provide funding. The rest of the authors declare no competing interests.

Additional information

Extended data is available for this paper at https://doi.org/10.1038/s41558-025-02537-1.

Supplementary information The online version contains supplementary material available at https://doi.org/10.1038/s41558-025-02537-1.

Correspondence and requests for materials should be addressed to Ann-Sofie P. Zinck.

Peer review information *Nature Climate Change* thanks Winnie Chu, Tyler Pelle and the other, anonymous, reviewer(s) for their contribution to the peer review of this work.

https://doi.org/10.1038/s41558-025-02537-1

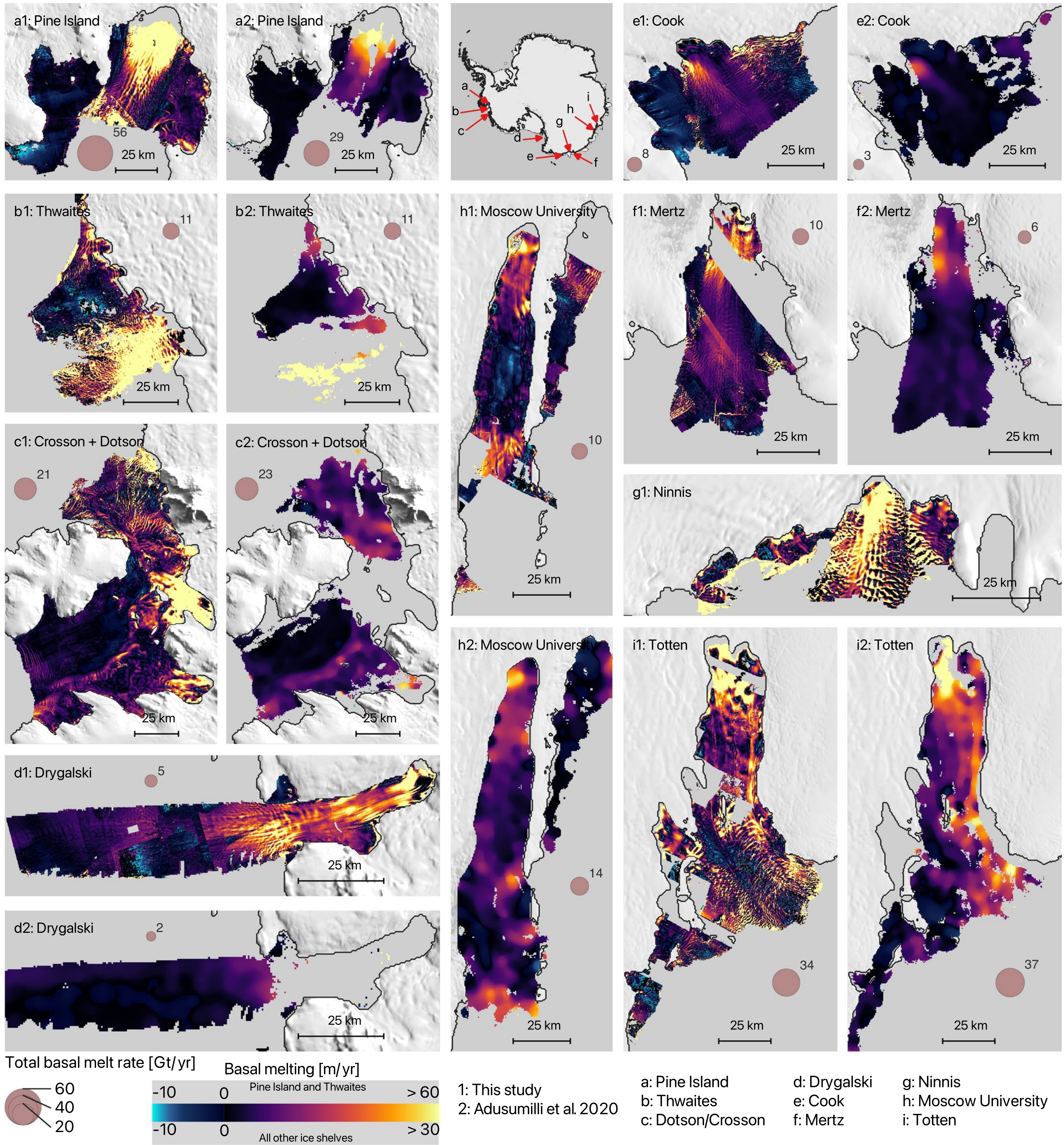

Extended Data Fig. 1 | Basal melt rate comparison. Basal melt rates from this study are marked with 1 and melt rates from Adusumilli7 are marked with 2. Panels **a**–**i** show the individual ice shelves as marked in the bottom legend. The Ninnis ice shelf (g) is not covered by Adusumilli[7]. The black line denotes the BedMachine V3 grounding line[43]. The circles denote total ice-shelf wide basal melt rate in Gt/yr, only considering areas covered by both BURGEE, Adusumilli[7], and Davison[8]. Note that, for example, different acquisition times (Suppl. Fig. 9) and radar penetration depth, can cause visible seams in the BURGEE melt maps (Supplementary Information S1). All panels use MODIS[50] as background imagery and are generated using Quantarctica[51]. The Quantarctica package is published under a Creative Commons Attribution 4.0 International License.

https://doi.org/10.1038/s41558-025-02537-1

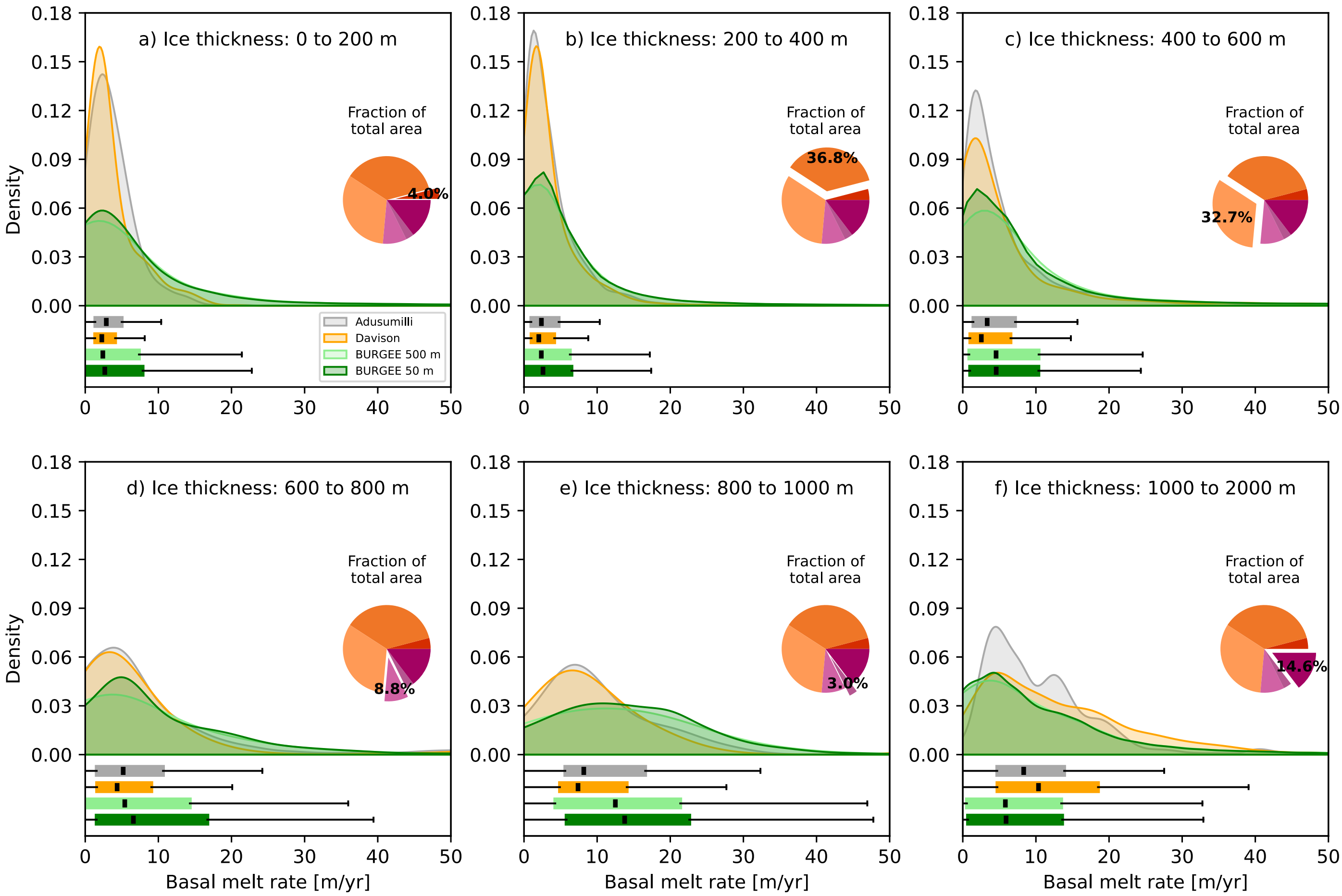

Extended Data Fig. 2 | Basal melt rate distributions. Basal melt rate probability density functions of Adusumilli[7], Davison[8], and BURGEE melt rates, the latter at the original 50 m posting and interpolated (nearest-neighbour) onto the 500 m grid used in Adusumilli[7]. Distributions are grouped by different ice shelf thickness sections based on BedMachine V3[43] and only areas covered by all melting products are considered (thus excluding Ninnis Ice Shelf). In the lower subpanels, the thick, vertical black line represents the median melt rate, the solid box ranges from the first to the third quartile, and the whiskers extend the box to 1.5x the inter-quartile range. The total area considered is 19,539 km^2, which in pixels correspond to 19,539 for Davison[8], 84,382 for Adusumilli[7] and BURGEE 500 m, and 7,801,438 for BURGEE 50 m.

https://doi.org/10.1038/s41558-025-02537-1

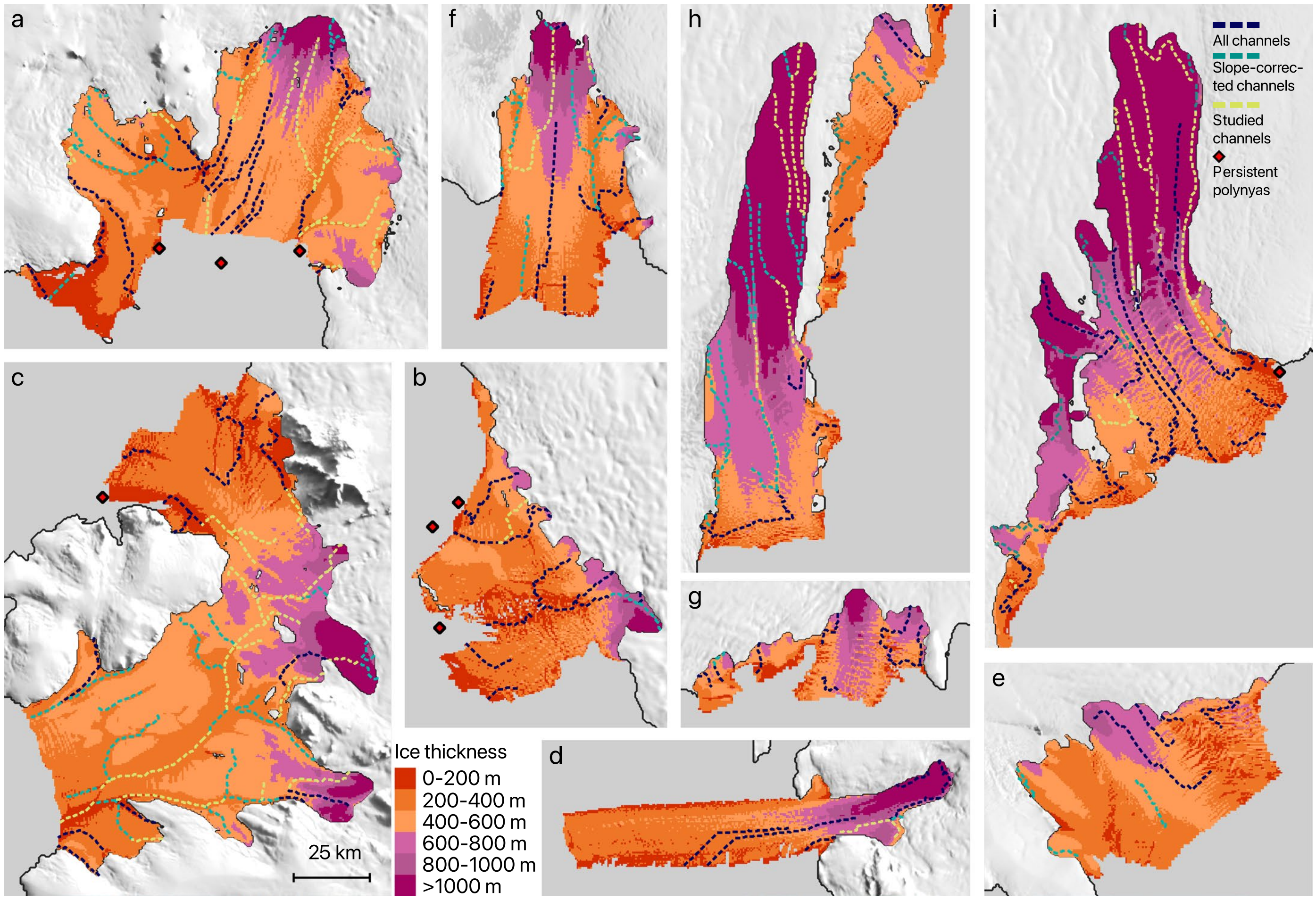

Extended Data Fig. 3 | Ice thickness and basal channels. a–**i**, BedMachineV3 ice thicknesses[43] overlaid with detected channels ('all channels') of Pine Island (**a**), Thwaites (**b**), Dotson/Crosson (**c**), Drygalski (**d**), Cook (**e**), Mertz (**f**), Ninnis (**g**), Moscow University (**h**) and Totten (**i**) ice shelves. All detected channels are further sub-categorized into slope-corrected channels which represent channels with maximum slopes < 15°. Only a subset of the slope-corrected channels is studied ('studied channels`), namely those channels where the 90% percentile melt rate is > 10 m/yr, as they are considered to be "active" melt-channels. Persistent polynya locations from ref. 24 are marked by red diamonds. Lettering corresponds to Extended Data Fig. 1. The solid black line denotes the BedMachine V3 grounding line[43]. All panels use MODIS[50] as background imagery and are generated using Quantarctica[51]. The Quantarctica package is published under a Creative Commons Attribution 4.0 International License.

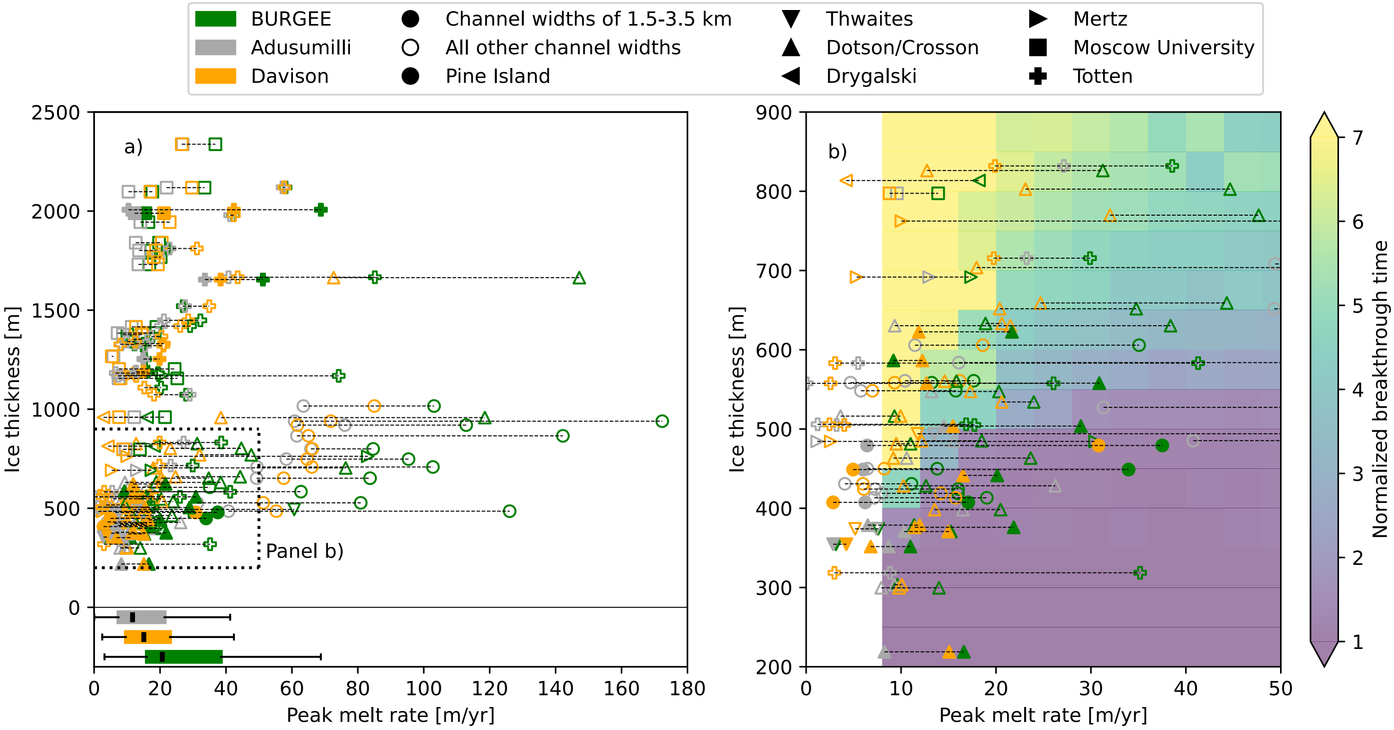

Extended Data Fig. 4 | Channel peak melt rates and normalized breakthrough times (NBTs). **a**) Channel peak melt rates compared to ice shelf thicknesses outside the channels. Dashed lines connect peak melt rates from the different products of the same channel. Filled markers indicate channels with a characteristic channel width of 1.5-3.5 km, which is comparable to the characteristic channel width (2.5 km) used to obtain NBTs[17]. Unfilled markers represent all other channels (only narrower). Dashed square marks the zoomed-in region in **b**). In the lower subpanel, the thick, vertical black line represents the median peak melt rate, the solid box ranges from the first to the third quartile, and the whiskers extend the box to 1.5x the inter-quartile range. The box plots are based on 88, 107, and 108 (sub-)channels for Adusumilli[7], Davison[8], and BURGEE, respectively. **b**) Zoom-in of channel peak melt rates compared to ice shelf thicknesses outside the channels and NBTs obtained from ref. 17. An NBT of 1 is when linear breakthrough and breakthrough with secondary flow are equal. Linear breakthrough times are shown in Suppl. Fig. 7.